Remapping of adult-born neuron activity during fear memory consolidation in mice

(恐怖記憶の固定化における成体新生ニューロンの活動

リマッピング)

２０２１

筑波大学大学院博士課程人間総合科学研究科

Vergara García Pablo Ismael

Remapping of adult-born neuron activity during fear memory consolidation in mice

(恐怖記憶の固定化における成体新生ニューロンの活動

リマッピング)

２０２１

筑波大学大学院博士課程人間総合科学研究科

Vergara García Pablo Ismael

筑　波　大　学

博 士 （ 医 学 ） 学 位 論 文

1. Table of contents

2. List of Abbreviations

ABNs	Adult-born neurons
AP	Anterior-posterior
CA	Cornus ammonis
CaM	Calmodulin
CC	Conventional CNMF-E
CNMF-E	Constrained non-negative matrix factorization for microendoscopic data.
CORR	Local correlation of a pixel and its neighbors
Cos	Cosine similarity
cpEGFP	Circularly permuted enhanced green fluorescent protein
DBNs	Developmentally-born neurons
DG	Dentate gyrus
DNA	Deoxyribonucleic acid
DV	Dorsal-ventral
EEG	Electroencephalogram
EMG	Electromyogram
GABA	Gamma-Aminobutyric acid
GC mice	Rosa26-pCAG-loxP-stop-loxP(LSL)-GCaMP3
GFP	Green fluorescent protein
ML	Medial-lateral
Nestin mice	pNestin-CreER^{T2}
NREM	Non-rapid eye movement
OB	Overlapping batches
PC	Pre-conditioning
PNR	Peak-to-noise ratio
postC	Post-conditioning
postS	Post-shock
preS	Pre-shock
PV	Parvalbumin
REM	Rapid eye movement
RI	Remapping index
SOM	Somatostatin
WT	Wild type
ZT	Zeitgeber time

3. List of figures

4. Abstract

In the hippocampal dentate gyrus, new granule cells are produced throughout the lifetime of mammals. Immature adult-born neurons (ABNs) are more excitable, less coupled to inhibitory circuits, and more plastic than other granules cells, suggesting that these neurons have an important role in memory and learning. However, their specific function in these processes is unknown. To address this issue, I analyzed recordings of the Ca^{2+} activities of individual ABNs throughout a contextual-fear conditioning memory paradigm. For this, I developed an algorithm that allows tracking the activity of individual ABNs across memory encoding, consolidation, and retrieval. ABNs were predominantly active when mice were exploring a novel environment. I found that fear learning did not recruit a distinct population of ABN. In sharp contrast, a completely different ABN population was recruited during fear memory retrieval. This was caused by the progressive remapping of ABN activities during the memory consolidation period. On the one hand, these results indicate that ABNs do not hold the putative properties expected for engram cells, since different populations were active during memory encoding and retrieval. On the other hand, this remapping of activities may serve ABNs to segregate memories encoded at different times. These results provide new insights into how ABNs operate during memory processing.

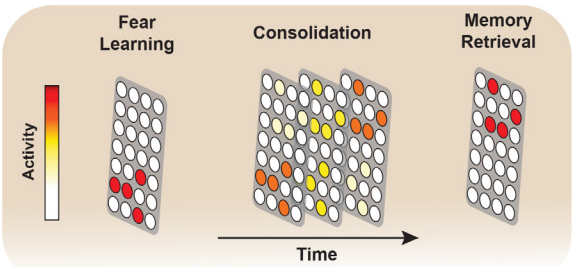

Graphical Abstract

5. Introduction

5.1. The unique properties of the young ABNs in the dentate gyrus.

Adult-born neurons (ABNs) in the dentate gyrus (DG) are constantly being integrated into the hippocampal circuit (Altman, 1963). These ABNs undergo a process of maturation that ultimately leads to synaptic and electric properties that are equivalent to those of developmentally born granule cells (DBNs) (Esposito, 2005; Praag et al., 2006; Stone et al., 2011). However, when ABNs are still immature, they display properties that largely differ from their mature counterparts, such as increased synaptic plasticity and excitability (Esposito, 2005; Ge et al., 2007; Gu et al., 2012; Schmidt-Hieber et al., 2004), and weaker inhibitory inputs (Alvarez et al., 2016; Groisman et al., 2020) (Figure 1).

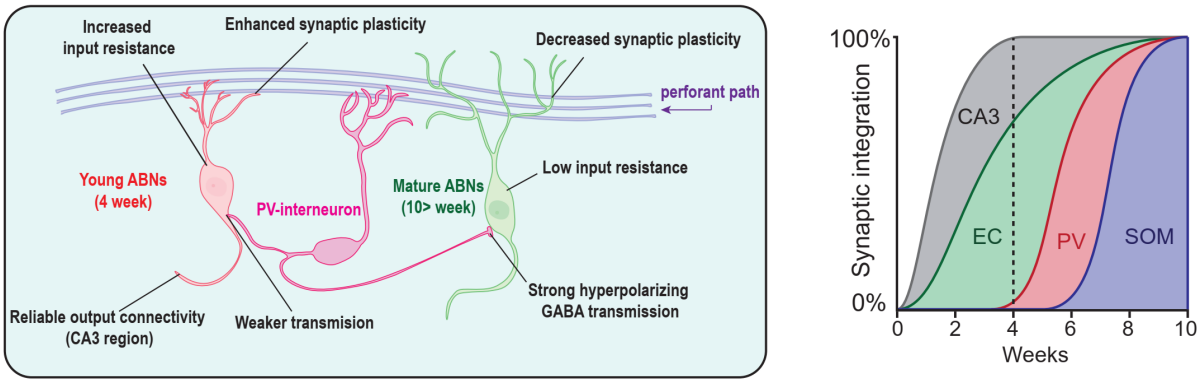

Figure 1. Synaptic and intrinsic properties of young adult-born neurons vs. mature neurons in the dentate gyrus. Behavioral data suggests a critical period for 4-week-old adult-born granule cells on memory processing. Mature granule cells and young ABNs display comparable output connectivity onto excitatory and inhibitory neurons in the CA3 region; however, young ABNs display increased amplitude and decreased induction threshold for long-term potentiation at input and output glutamatergic synapses. Moreover, their input resistance is around two-fold higher than mature granule cells, meaning that similar synaptic inputs are translated into larger voltage fluctuations. Young ABNs also receive weaker feedback and feedforward inhibition from parvalbumin (PV) and somatostatin (SOM) interneurons, while receiving modestly developed entorhinal cortex glutamatergic inputs. This is translated into a larger excitation/inhibition balance in comparison to mature neurons.

These properties may bestow ABNs with unique roles during memory processing; indeed, several studies indicate that ABNs contribute to each of the three main stages of memory: encoding, consolidation, and retrieval (Arruda-Carvalho et al., 2011; Danielson et al., 2016; Gu et al., 2012; Kumar, Vergara, et al., 2020; Shors et al., 2001). We have recently found that the ABNs activity during REM sleep is necessary for memory consolidation (Kumar, Vergara, et al., 2020) (Figure 2). By imaging the Ca^{2+} activity of ABNs (Figure 3) in sleeping mice during memory consolidation, we found that, overall, ABNs become less active during rapid-eye-movement (REM) sleep after mice form a fear memory consisting of an association between a context and shock but not after they are exposed to context or shock alone. Interestingly, the fraction of ABNs that were active during REM sleep were predominantly related to the reactivation of ABNs that were active during learning. Disruption of ABNs activity during REM sleep by optogenetic activation or inhibition led to memory impairments, demonstrating that the sparse activity of ABNs during REM sleep is necessary for memory consolidation, at least in mice.

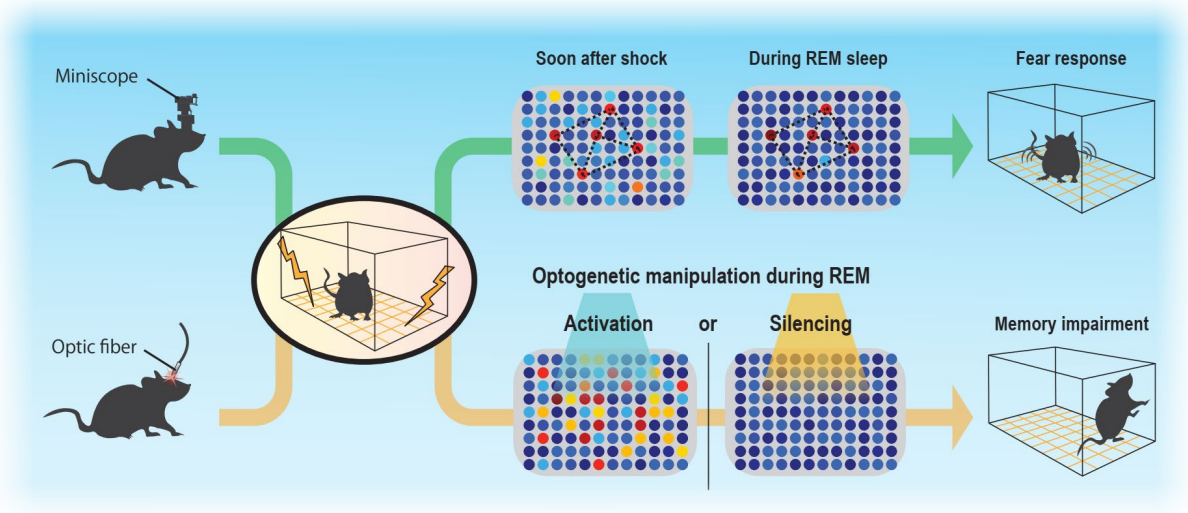

Figure 2. Sparse activity of ABNs during REM sleep is necessary for memory consolidation. Contextual fear conditioning recruits a subset of ABNs that reactivate in subsequent REM sleep. Disruption of ABNs activity during REM sleep by optogenetic activation or silencing impairs memory consolidation.

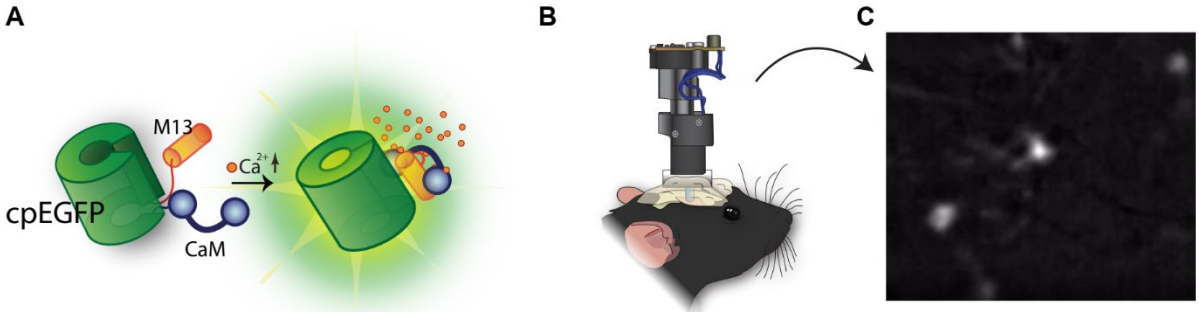

Figure 3. Imaging Ca^{2+} activity through GCaMP sensors. (A) Ca^{2+} imaging uses genetically encoded Ca^{2+} sensors (such as GCaMP) to monitor the Ca^{2+} activity of neurons. Action potentials trigger Ca^{2+} influx through voltage-gated Ca^{2+} channels producing a 10 to 100 fold increase in Ca^{2+} concentration inside a neuron (Berridge et al., 2000). Therefore, the spiking activity of a neuron can be inferred by monitoring its internal Ca^{2+} concentration (although other sources of Ca^{2+} may hinder this estimation). The GCaMP sensors are composed of a circularly permuted enhanced GFP (cpEGFP) attached to the calcium-binding protein calmodulin (CaM) and the CaM-binding peptide M13. In the absence of Ca^{2+}, cpEGFP is in a non-fluorescent state. When Ca^{2+} concentrations are high, the CaM hinge region binds to the M13 peptide triggering a conformational change of cpEGFP. In this conformation, cpEGFP displays bright fluorescence in response to blue light stimulation. (B) Using a miniature microscope (microendoscope) mounted on the mouse head and a gradient-index implanted above target neurons, the activity of several neurons, genetically modified to express GCaMP, can be monitored. (C) A representative field of view captured with a microendoscope (after processing the signal) in GCaMP3-expressing ABNs.

5.2. Are ABNs engram cells?

The ABNs contribute to memory encoding, consolidation, and retrieval; however, the exact mechanism by which ABNs contribute to each of these stages is unknown. One possibility is that ABNs operate as engram cells (Semon, 1921; for a review see: Josselyn & Tonegawa, 2020) (Figure 4). The fact that animals can recall a previous experience suggests that an internal representation of this experience is stored in the brain. The term “engram” refers to the neural substrate that constitutes this representation of a memory. Engrams operate by two fundamental principles: the first principle is the law of engraphy (Figure 4A), which posits that the simultaneous activation of neural ensembles during learning binds these ensembles together, which forms an interconnected network that constitutes the engram. For example —in a

classic contextual-fear conditioning memory paradigm— the engram storing the context-fear association is formed by the synaptic interconnection created by the simultaneous activation of the neurons responding to the explored context (green circles in Figure 4) and the neurons responding to the shock (red circles in Figure 4). The second principle is the law of ekphory (Figure 4B), which posits that the reactivation of some of the engram neurons in response to a stimulus presented during learning, leads to the complete reactivation of the engram, as a result of the interconnectivity of the circuit. For example, re-exposure to the conditioned context triggers the activation of not only the neuron that intrinsically respond to this stimulus but also the neurons that were previously activated by the shock experience. Collectively, both principles constitute the hypothetical mechanism of memory association.

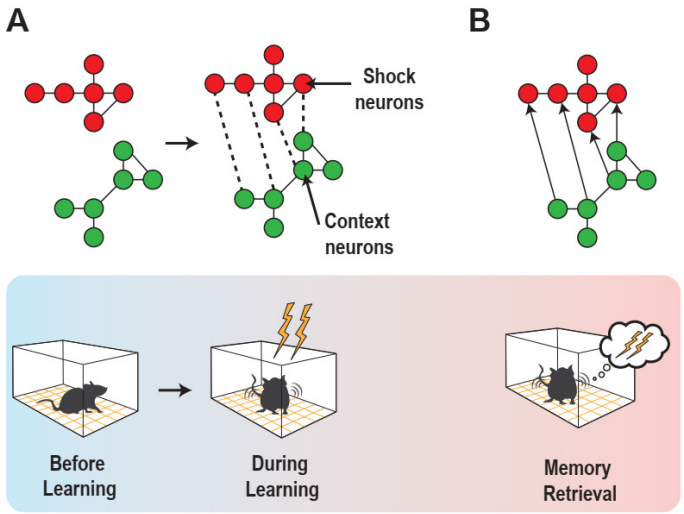

Figure 4. Activity dynamics of engram cells. (A) Law of engraphy, operating during memory formation (B) Law of ekphory, operating during memory retrieval.

5.3. Ca^{2+} imaging in ABNs.

Monitoring the activity of single neurons *in vivo* is fundamental for understanding the brain mechanisms of memory and learning. If ABNs operate as engram cells, then

their activity dynamics should satisfy at least two conditions: 1) A specific population of ABNs should be activated during learning, and 2) this same population should be reactivated when animals remember the encoded memory. To address these two points, it is necessary to accurately estimate ABNs activity throughout memory processing. Traditionally, neural activity has been monitored by electrodes acutely or chronically implanted in the brain. These electrodes are used to record “spikes” corresponding to the action potential of single neurons. Different features of these spikes (amplitude, width, etc.) are then used to segregate and classify the spikes corresponding to different neurons, a process that is known as spike sorting (Rey et al., 2015). Spike features can also be used to segregate different neural types, such as excitatory neurons from fast-spiking interneurons; however, for populations of neurons with similar spike dynamics but different molecular profiles —as occurring with ABNs and other granules cells— spike segregation is not possible. To tackle this limitation, we expressed the Ca^{2+} sensor GCaMP3 in ABNs (Figure 3). Although more recent indicators, such as GCaMP6 variants, are usually preferable, their transgenic lines (Madisen et al., 2015) show very low or absent expression in ABNs (see the specific transgenic lines used in Figure 10 and methods). Indeed, Kumar et al., tested several versions of GCaMP, including GCaMP3, 6s, 6f, 7f, and 8, but only GCaMP3 showed consistent expression in young ABNs. We speculate that the expression of recently developed GCaMP sensors in early neural progenitors interferes with Ca^{2+} signaling mechanisms essential for immature ABN survival.

One of the biggest limitations of Ca^{2+} imaging is its limited temporal resolution in contrast to electrophysiological approaches: while electrophysiological data is usually sampled within kilohertz resolution, Ca^{2+} imaging in freely behaving mice is usually sampled within 5 to 30 frames/s (Aharoni et al., 2019; Ghosh et al., 2011). This

temporal resolution is limited to the temporal dynamics of the Ca^{2+} sensors (Rising time: ~95ms. Decay time: 650ms, for GCaMP3 (Tian et al., 2009)), which is several orders of magnitude slower than the duration of a single spike (in the order of 1ms). Although the specific timing of isolated spikes cannot be determined with millisecond resolution, we can still determine the number of spikes occurring in broader temporal windows (in the order of ~100ms). This is because the relationship between GCaMP3 fluorescence intensity and the number of action potentials occurring in a short period of time (1-2s) is approximately linear when the number of consecutive action potentials is less than 10 (Tian et al., 2009). Although isolated action potential can be detected with GCaMP3 *ex vitro* (Tian et al., 2009), in *in vivo* recordings single spikes may not be reliably detected given the larger contribution of background fluctuations (contamination from surrounding neuropil and neurons outside the focal plane). Therefore, activity estimated by Ca^{2+} imaging may be biased to detect bursting activity over isolated spikes. However, burst activity is often linked with relevant physiological functions in granule cells. For example, granule cells in the DG reliably activate postsynaptic neurons in CA3 when they fire in bursts, but not through isolated spikes (Henze et al., 2002). Moreover, burst activity may specifically drive synaptic plasticity in hippocampal neurons (Thomas et al., 1998), including granule cells (Orr et al., 2001).

5.3.1. Processing Ca^{2+} imaging data.

The algorithm used to extract the neural signal would depend on whether a one-photon or a two-photon microscope is used (Figure 5). Overall, two-photon microscopes have better resolution and cause less bleaching than one-photon microscopes; however, miniaturize two-photon microscopes are not currently commercially available. In contrast, there are several open-source projects (Aharoni & Hoogland, 2019; Srinivasan, Vergara, et al., 2019) and commercially available miniaturized one-photon

microscopes (Inscopix, Palo Alto, USA; Doric, Québec, Canada). Despite the resolution differences between two- and one-photon microscopes, the somatic Ca^{2+} signals extracted by both methods display similar properties (Glas et al., 2019). Additionally, miniaturized one-photon microscopes allow monitoring the activity of ABNs in freely behaving animals, whereas recordings with two-photon microscopes require head-fixed animals. This can importantly reduce stress in mice (Juczewski et al., 2020), which affects memory and REM sleep dynamics (Moreira et al., 2016; Nollet et al., 2019). Considering the active role of ABNs in REM sleep and memory processing, we opted for 1-photon miniaturized microscopes.

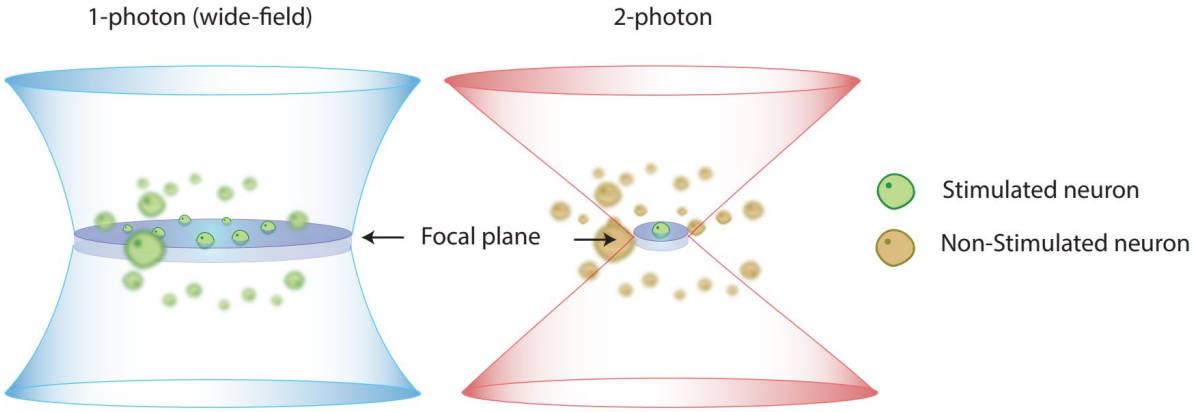

Figure 5. Ca^{2+} imaging with one-photon microscopy (wide-field) vs 2-photon microscopy. In one-photon imaging, the whole field of view is stimulated with blue light. This stimulates neurons inside and outside the focal plane, leading to the contamination of target regions with neural signals outside the focal plane. In two-photon imaging, two photons of light, with approximately twice the wavelength used in one-photon imaging, are used to excite GCaMP. Instead of stimulating the whole field of view, a laser sequentially scans small segments within the field of view. This produces an image with reduced background contamination from neurons outside the focal plane and higher spatial resolution than one-photon imaging. Additionally, the use of larger wavelengths increases tissue penetration and decreases bleaching. The main disadvantage of two-photon imaging is the lower sampling rates compared to one-photon imaging. Also, two-photon miniaturized microscopes are not currently commercially available, therefore recordings in freely behaving animals are currently restricted to one-photon imaging.

Before extracting the neural signals from the Ca^{2+} imaging video, it is necessary to align each frame in the video to a common reference frame to correct artifacts arising

from brain motion. State-of-the-art algorithm (Pnevmatikakis & Giovannucci, 2017) can correct brain motions in most cases, but not all of them (Figure 6).

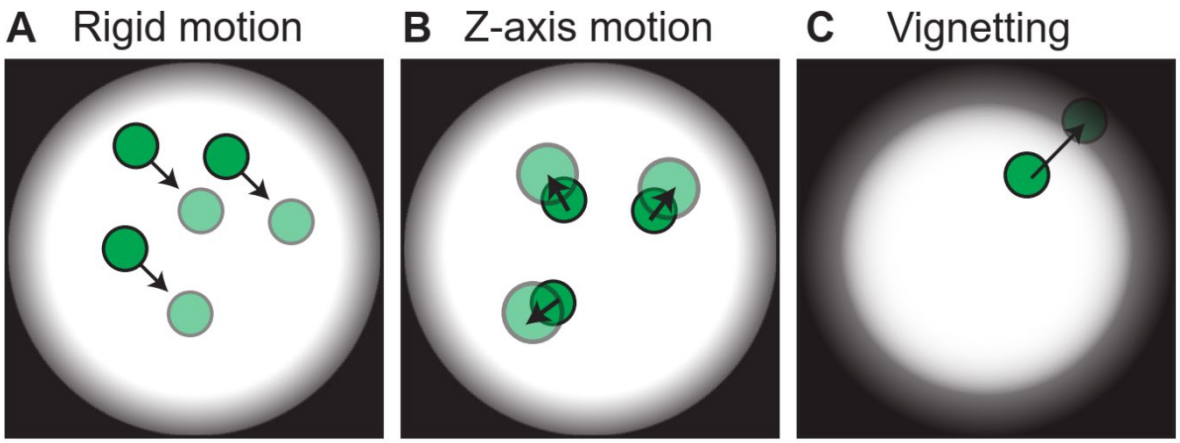

Figure 6. Motion correction algorithms may solve some, but not all the problems associated with motion. (A) Rigid motion occurring as uniform displacement in the XY-axis can be automatically corrected by most motion correction algorithms. (B) Modest movements in the z-axis can be corrected by non-rigid motion correction algorithms (Pnevmatikakis & Giovannucci, 2017) or by a rigid motion correction algorithm implementing expansions and rotations (MOSAIC software, Inscopix). However, correcting this type of motion may require manual parameter tunning and may not be corrected automatically in some cases. (C) Even if the frames of a video are correctly aligned, changes in the stimulation intensity caused by vignetting (reduction of an image's brightness toward the periphery) may not be corrected, especially if the movement of the brain is desynchronized with the movement of the microscope.

After motion correction, neurons' locations and their fluorescence traces are extracted from the motion-corrected data. The most widely used algorithm to extract Ca^{2+} signal from one-photon imaging data is constrained non-negative matrix factorization for microendoscopic data (CNMF-E) (Zhou et al., 2018). Briefly, CNMF-E operates on the notion that the whole video recording can be expressed as the product of a spatial matrix corresponding to the spatial footprint of each neuron and a temporal matrix that characterizes the Ca^{2+} concentration of each neuron over time. This model is further enriched to handle one-photon imaging by also modeling the high background fluctuation caused by fluorescent signals outside of the focal plane. To properly extract the Ca^{2+} traces, CNMF-E requires an initial approximate estimation of the shape and location of neurons (i.e., initialization). The general approach used by CNMF-E is to

calculate the local correlation of a pixel and its neighbors (CORR), and the peak-to-noise ratio (PNR) of each pixel from the whole video file (Figure 7). Intuitively, pixels corresponding to active ABNs would display higher CORR and PNR values than pixels that do not correspond to active neurons.

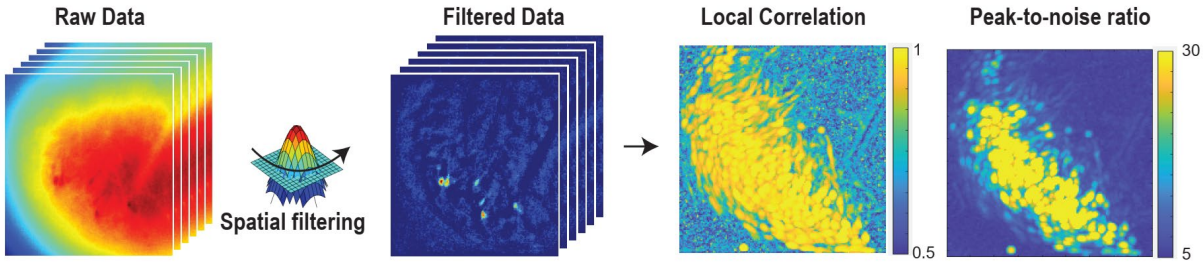

Figure 7. Initialization of neurons by CNMF-E. The figure represents a stack of images obtained from granule cells data. Each frame in the stack is first spatially filtered to enhance circular regions (i.e., neuron shapes) and reduce larger background fluctuations. From this filtered stack we calculate a local correlation image (the correlation between neighbor pixels) and a peak-to-noise ratio image. These two images are then thresholded to identify pixels associated with candidate neurons.

Although these parameters may serve to roughly estimate the location and spatial shapes of neurons in most experimental conditions, for long recordings—as occurring in this study— performance is drastically decreased. This happens because, in one-photon imaging, pixels associated with a neuron are highly correlated only when that neuron is active (Figure 8). Given that ABNs are most of the time inactive, increasing the video length would be asymptotically translated into a lower CORR. To solve this problem, I propose an overlapping batches approach: instead of analyzing the whole video sequence, the video is divided into small overlapping batches. This allows estimating the spatial components of ABNs from discrete temporal windows of maximum neural activity (Figure 9).

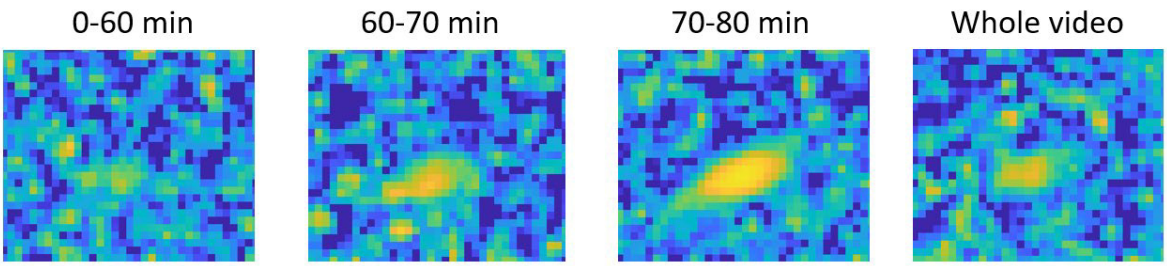

Figure 8. CORR images of an ABN in different time windows. In one-photon imaging, the pixels constituting a neuron are only highly correlated when that neuron is active. However, granule cells of the dentate gyrus are most of the time inactive (Diamantaki et al., 2016), a property that is shared with ABNs. For example, the ABN shown in the figure only shows a prominent local correlation in the last 10 minutes of an 80-minutes-long recording session. If the CORR imaging is calculated using the whole video session, then this neuron would end up undetected.

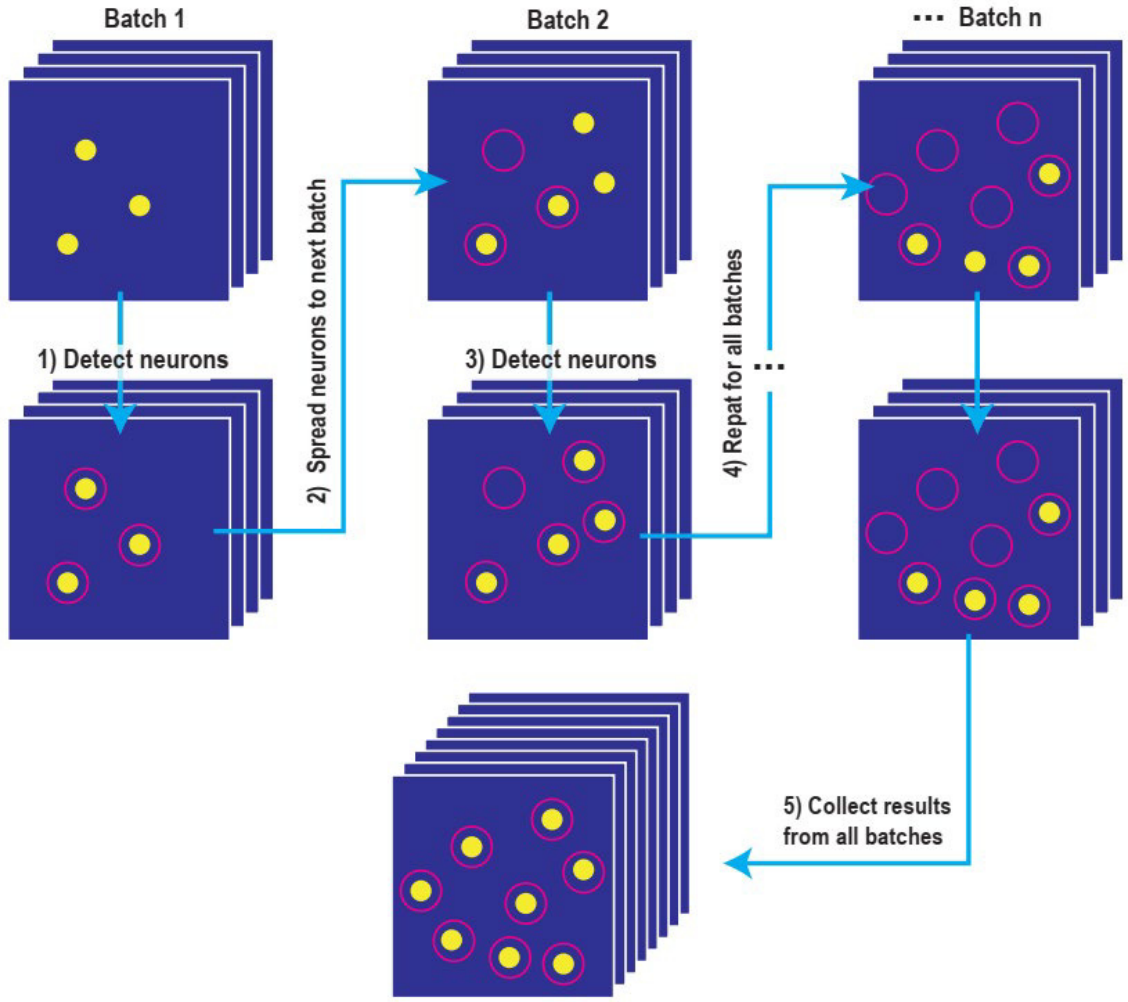

Figure 9. Overlapping batch implementation of CNMF-E for the analysis of lengthy Ca^{2+} imaging data. The video is initially distributed into n batches, which are analyzed through the following pipeline: (1) Neurons are detected in the first batch using the standard CNMF-E implementation (yellow circles

represent active neurons. Magenta circles indicate detected neurons). (2) Following, the neurons detected in batch #1 are spread into batch #2. Because the activity of neurons may change, some neurons may appear inactive or display very little activity in subsequent batches (e.g., Magenta circles without yellow circles in batch #2). Similarly, neurons that were initially inactive may become active in subsequent batches (new yellow circles). (3) Therefore, in each batch new neurons are searched and included. (4) The same process is repeated until all batches are analyzed. (5) Finally, the data collected across all batches are grouped together.

6. Research Question, Hypothesis, and Objectives.

Research question: What is the mechanism by which ABNs mediate memory?

Hypothesis: ABNs mediate memory by operating as engram cells.

Objective: Determine whether the activity dynamics of ABNs during memory encoding, consolidation, and retrieval are compatible with the activity dynamics expected for engram cells.

7. Results

7.1. Experimental Design.

I analyzed the activity of ~4-week-old ABNs in pNestinCreERT2/pCAG-LSL-GCaMP3 mice throughout the course of a contextual fear conditioning paradigm (Kumar, Vergara, et al., 2020) at a population level. Recordings were performed over three major consecutive periods: learning, consolidation, and retrieval (Figure 10). Immediately after a recording session in a familiar environment (pre-conditioning in the home cage, preC; 10 min), the learning period included recording sessions in a conditioning context before foot shock (pre-shock in context A, preS; 10 min), and the same context after foot shock (post-shock in context A, postS; 5 min). In the consolidation period, mice stayed in their home cage for a total of 5.5 h, and recording was performed in the final 2.5 h. During this period, memory consolidation depends on the sparse activity of ABNs during rapid eye movement (REM) sleep (Kumar,

Vergara, et al., 2020). In the post-consolidation period, mice were re-exposed to context A (test; 10 min), during which they exhibited context-specific freezing behavior (Kumar, Vergara, et al., 2020).

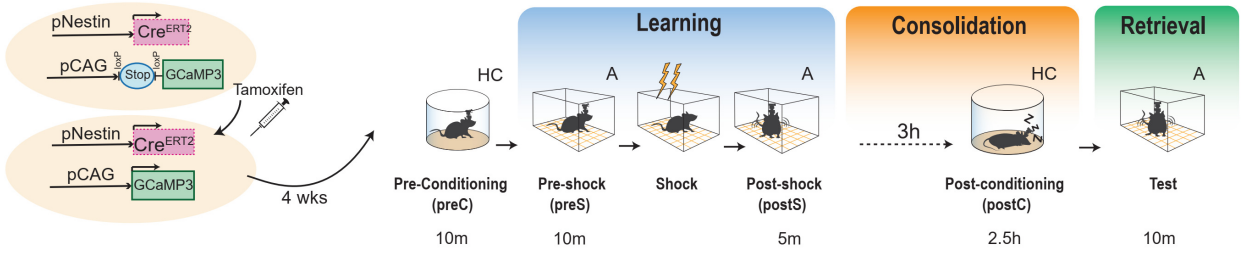

Figure 10. Experimental design. Left: Doble transgenic setup used to express GCaMP3 specifically in ABNs. In baseline conditions, a stop sequence located after the pCAG (a constitutive promoter) prevents the expression of GCaMP3. The CreER^{T2} recombinase, which is expressed only in progenitor cells (by Nestin promoter), is translocated to the nuclear compartment only after Tamoxifen injection. This translocation causes the excision of the stop sequence (by recombination of two *loxP* sequences flanking the stop codon). Right: Four weeks after tamoxifen injection, mice were subjected to a fear conditioning paradigm. The activity of ABNs was monitored throughout the learning, consolidation, and retrieval of this contextual fear memory (see methods for detail).

7.2. Extraction of Ca^{2+} traces from individual ABNs.

Determining the activity dynamics of ABNs across all the recording sessions requires tracking the activity of individual ABNs. To extract the spatial and temporal structure of neurons I implemented an overlapping batching (OB) approach for the original CNMF-E algorithm (Zhou et al., 2018) (Figure 9, Figure 11). The main advantage of the overlapping batch implementation is that it allows detecting neurons overall displaying low activity but high activity over brief periods (e.g., a neuron that is only active during learning but remains inactive in the following hours during memory consolidation and sleep). This is depicted in Figure 11A, in which the CORR and Ca^{2+} transients of three close ABNs are shown for three consecutive batches. Note that ABNs display prominent Ca^{2+} transients that translate into a higher CORR (above the detection threshold), particularly in the third batch. Because the spatial component of

each neuron is shared across batches, only the third batch is necessary to initialize those ABNs, even if other batches have CORR comparable to the background level. Having obtained a good initial estimation of the spatial components, the CNMF-E algorithm can extract temporal traces from other batches, even if its CORR or PNR is below the defined threshold. An overlapping batch approach produces a cleaner estimation of CORR, in contrast to the analysis of the entire video sequence (Figure 11B). In some cases, artifacts are introduced in the concatenation point between batches. Thus, I implemented a multi-batch algorithm using 50% overlap. This approach can extract reliable Ca^{2+} traces from ABNs in most cases. To illustrate the differences between the OB method and the conventional CNMF-E (CC) method (i.e., running CNMF-E on the whole video sequence), I compared the spatial and temporal components extracted by both methods (Figure 11C). True-positive neurons are expected to display circular shapes and Ca^{2+} transients distinguishable from noise. Neurons extracted by the OB method display higher circularity and PNR than those extracted by the CC method (Figure 11D). Indeed, several neurons extracted by the CC method display spatial components that largely differ from a circular shape. Considering those spatial components with circularities five standard deviations below those extracted by the OB method, I estimated that 34% of components extracted by the CC method are false positives (Figure 11D, left, red dots). Next, I examined how the final temporal and spatial components of the transients extracted by the OB or CC method (analysis of >30,000 frames) differ from those extracted from the analysis of an individual batch (analysis of ~1,000 frames) (Figure 11E). Components extracted by the OB method were spatially and temporally more similar to those extracted from an individual batch (Figure 11F). Furthermore, I estimated that, on average, 61% of neurons remain undetected in each batch (compared with the total neurons found in

the OB method) (Figure 11G, left). This happens because most of the active ABNs display PNR significantly below the detection threshold (Figure 11G, right). These results indicate that the OB method minimizes the number of false positives without compromising true-positive detection.

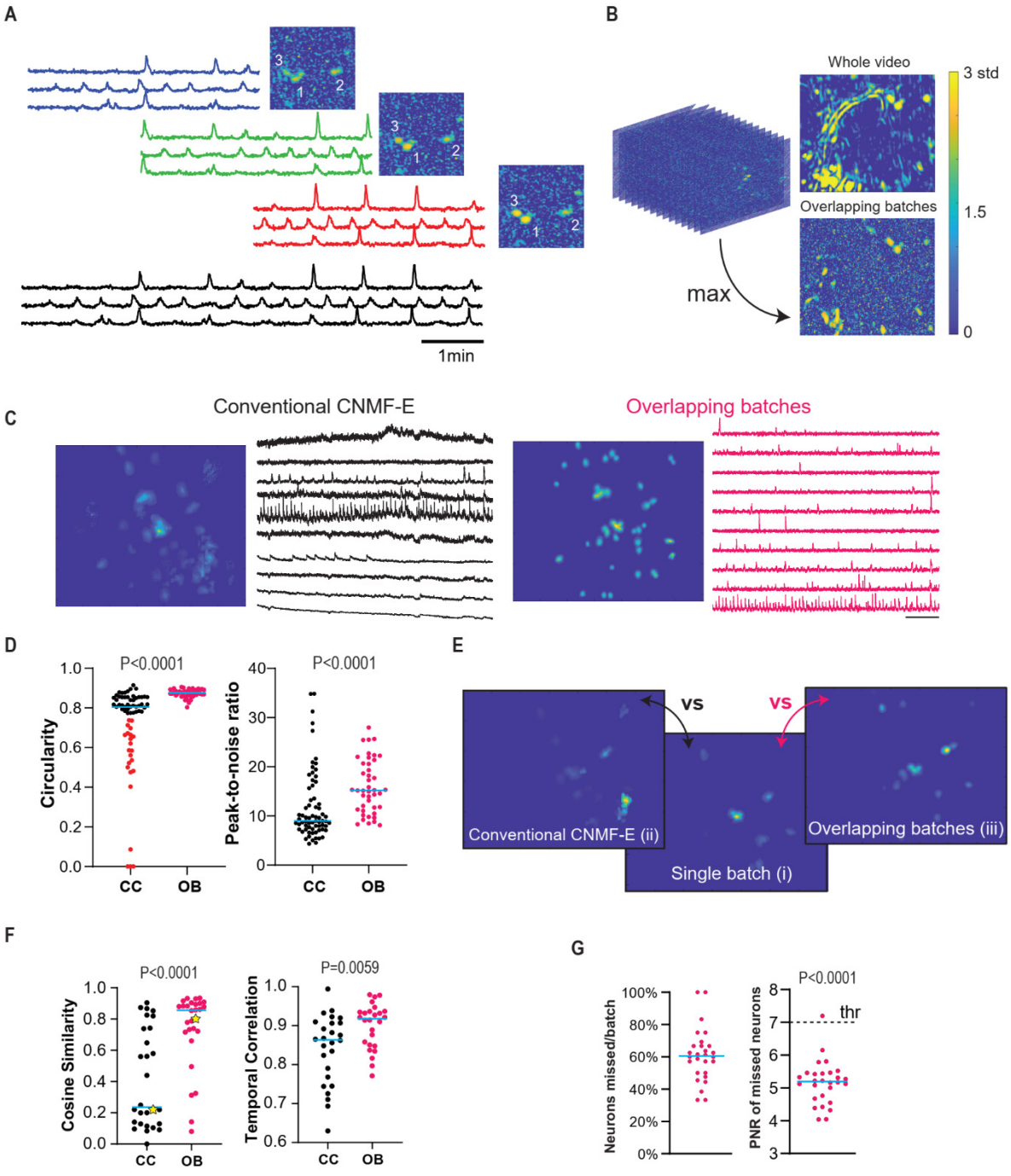

Figure 11. Analysis of Ca^{2+} imaging data. (A) Ca^{2+} transients detected and CORR for three neurons in three consecutive batches. Black trace shows the final estimated signal for the entire recording.

(B) Normalized CORR for a 3-h video obtained by analyzing the entire video sequence versus the maximum projection of the CORR images obtained by the overlapping batch implementation. Note that CORR of the entire video sequence includes many highly correlated non-circular shapes that are unlikely to represent real ABNs. Analysis of the entire video will introduce several false positives and noisier estimation of Ca^{2+} transients in this case. (C) Spatial and temporal features of Ca^{2+} transients extracted by conventional CNMF-E (CC) and overlapping batches (OB) methods. The two transients were randomly chosen from those extracted by CC or OB methods. (D) Circularities (isoperimetric quotient) of spatial components and PNR of temporal traces. (E) Example of spatial components extracted from an individual batch (i), the OB method (ii), or the CC method (ii) in the same time period. Because there are more neurons in the entire recording period than in an individual batch, spatial components were weighted by average activity during the period. (F) Left: Cosine similarity of spatial components for the individual batch versus CC method and individual batch versus OB method. The star symbol in the figure corresponds to the spatial components shown in (G). Right: Temporal correlation of Ca^{2+} transients of common neurons for the individual batch versus CC method and individual batch versus OB method. A neuron extracted by the CC or OB method was considered to be the same as that in an individual batch if its spatial component had a cosine similarity >0.8. If more than two pairs of neurons satisfied this condition, the pair with the higher temporal correlation was used for calculations. (H) Left: percentage of active neurons not detected in an individual batch. Right: PNR of missed neurons. Data were analyzed by Mann-Whitney tests (D, F) and one-sample t-tests (G).

Previous reports indicate that ABN Ca^{2+} transients occur at very low rates (~1 transient/min) (Danielson et al., 2016; Kumar, Vergara, et al., 2020). However, each Ca^{2+} transient usually shows polyphasic dynamics (i.e., contains multiple peaks) (Fig. 4A), reflecting the integration of several unitary Ca^{2+} events. To precisely estimate the Ca^{2+} activity of ABNs, complex Ca^{2+} transients were decomposed into isolated events by deconvolution of the raw Ca^{2+} traces (Figure 12A) (Friedrich et al., 2017). To examine the temporal aggregation of these events, I calculated a mean circular autocorrelation function (Figure 12B), which provides an estimate of the likelihood of observing one event soon after another (Aljadeff et al., 2016). The autocorrelation function assumes a constant value when events are randomly distributed in time, as occurs when events are temporally shuffled (Figure 12B, green). By contrast, the autocorrelation function for actual events showed an exponential decay within 10 s (Figure 12B, red), suggesting that ABN activity is temporally aggregated.

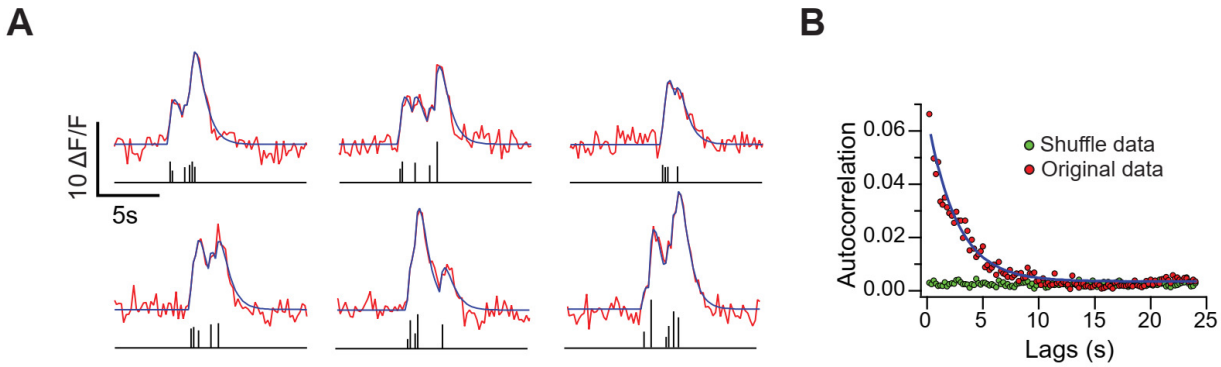

Figure 12. ABNs display burst-like activity. (A) Six examples of Ca^{2+} trace deconvolution. Raw signal (red, top) was decomposed into unitary Ca^{2+} events with amplitude (height) and timing information (bottom, black bars). Overlaying blue traces (top) show reconstructed Ca^{2+} signal. (B) Circular autocorrelation function of mean activity from actual data (red dots) and temporally shuffled data (green dots). The blue line is an exponential fit.

7.3. ABNs activity increase when mice explore a new context.

I found that the mean activity of ABNs increased when mice explored the fear conditioning context (Figure 13A-C). I estimate that ~28% of ABNs showed increased activity during the preS period (Figure 13C, top). However, event frequency returned to preC levels during the postS and test periods. Indeed, ~10% of the ABNs showed decreased activity after shock experience (i.e., preS to PostS, Figure 13C, bottom).

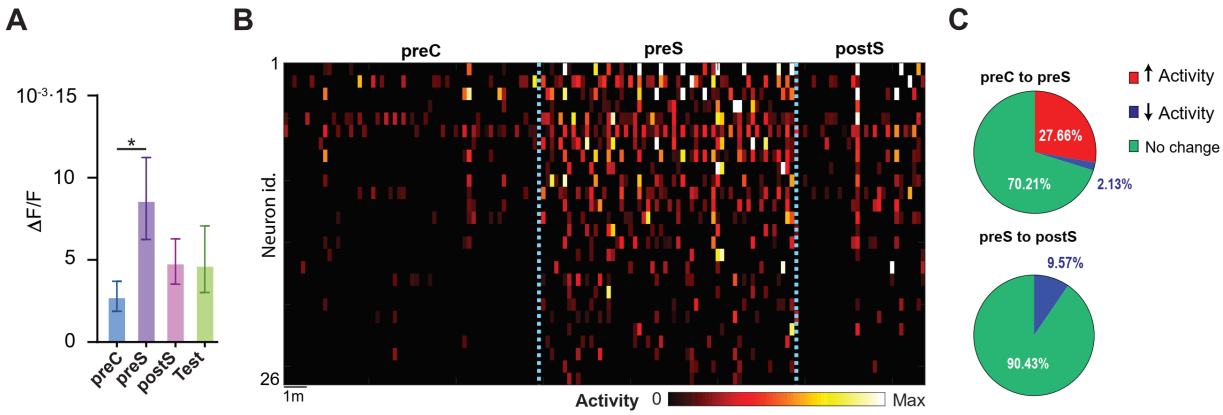

Figure 13. Adult-born neurons react to novel context encoding. (A) Mean Ca^{2+} activity in different contexts. Bootstrap, *p<0.05, n= 94 neurons from 4 mice (same sample size applies for all the figures in this manuscript). Error bars are 95% confidence interval (same applies for the rest of the manuscript) (B) Activity heatmaps of neurons significantly increasing their activities in the preS context. Block Bootstrap, *p<0.05. Each time bin is 10 s. (C) Pie chart of the ABNs responding to preS and postS.

7.4. ABNs active during learning do not overlap with the ABNs active during memory retrieval.

These observations of individual ABN activity, however, do not clarify whether a similar or different population of ABNs is recruited in different periods. For instance, a difference in activity could reflect the recruitment of a new population that is active in a specific period (Figure 14A, model 1) or a change in the activity of the same population (Figure 14A, model 2). To address this issue, I arranged the mean activities of individual ABNs into column vectors across different periods (Figure 14B, hereafter referred to as activity vectors). If a similar population of ABNs is recruited in two different periods, its activity will be correlated. I analyzed this possibility by creating a similarity matrix (i.e., cosine similarity) considering all possible comparisons between activity vectors (Figure 14C). Subsequent hierarchical clustering of this matrix revealed that a similar population of ABNs is active across the preC, preS, and postS periods, suggesting that neither novel context exposure nor shock experience recruits a different ABN population. Surprisingly, a different ABN population was predominantly active during the test period, suggesting that active ABN populations do not overlap between learning and retrieval. This phenomenon was detected in all the mice included in this study 14 Appendix 3).

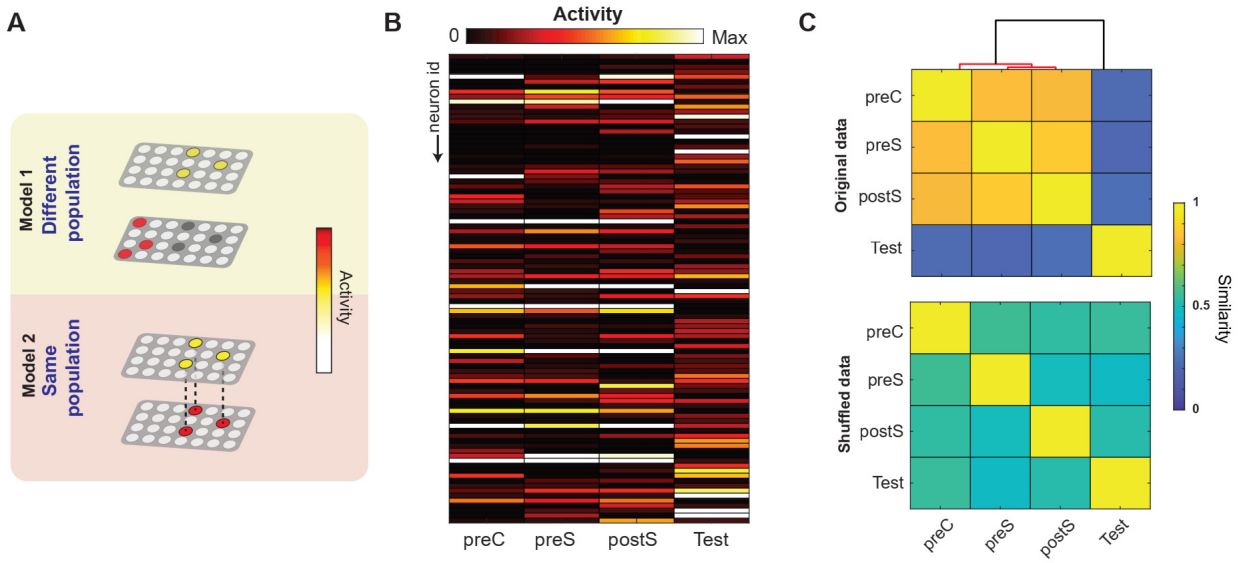

Figure 14. No overlap between ABN populations active during learning versus retrieval**.** (A) Two potential models by which population ABN activity could change between two different periods. (B) ABN activity vectors in different periods. Each row represents the mean activity of individual ABNs. Each activity vector was rescaled from 0 to 1. (C) Similarity matrix (i.e., cosine similarity) between pairs of activity vectors for the original data (top) and after random shuffling (bottom). The overlaying dendrogram represents the results of hierarchical clustering, with significant clusters ($p < 0.05$) shown in red.

7.5. ABNs remap during the consolidation period.

This segregation of ABN population activity may take place during memory consolidation. To address this possibility, I divided the consolidation period into 15-min bins and calculated an activity vector for each bin (Figure 15A). Next, I calculated a remapping index that indicates whether a given activity vector is closer to that at the beginning or end of the consolidation period. This remapping index ranges from -1 to 1; a value of 1 indicates a perfect match to the first bin of the consolidation period, a value of -1 indicates a perfect match to the last bin, and a value of 0 indicates equidistance from both. Remapping indices were strongly correlated with time, indicating that ABN activity gradually remapped during the consolidation period (Figure 15B). This remapping was detected regardless of whether mice were awake or asleep. It was not possible to calculate remapping indices during REM sleep given the limited

amount of REM sleep during the consolidation period (<10% of total time) and the sparse activity of ABNs during this sleep stage (<6% of total ABN activity occurs in REM sleep) (Kumar, Vergara, et al., 2020). Gradual activity remapping was detected in all recorded mice 14 Appendix 3).

Activity remapping may occur in all or a specific population of ABNs. To discern between these two possibilities, I traced ABNs with activities significantly correlated with time during the memory consolidation period. This revealed two subgroups of neurons, one gradually decreasing their activities, and another one increasing their activities (Figure 15C-D). The ABNs decreasing their activities were predominately active during the preS/postS periods; in contrast, the ABNs increasing their activities were predominantly active during the test period (Figure 15E). Accordingly, significant clusters in the similarity matrix were only detected for the ABNs that showed significant changes in activity during consolidation and not among those that showed no correlation (Figure 15F). Collectively, these results suggest that the populations of ABNs that are active during fear learning and retrieval are segregated over time by an activity remapping process.

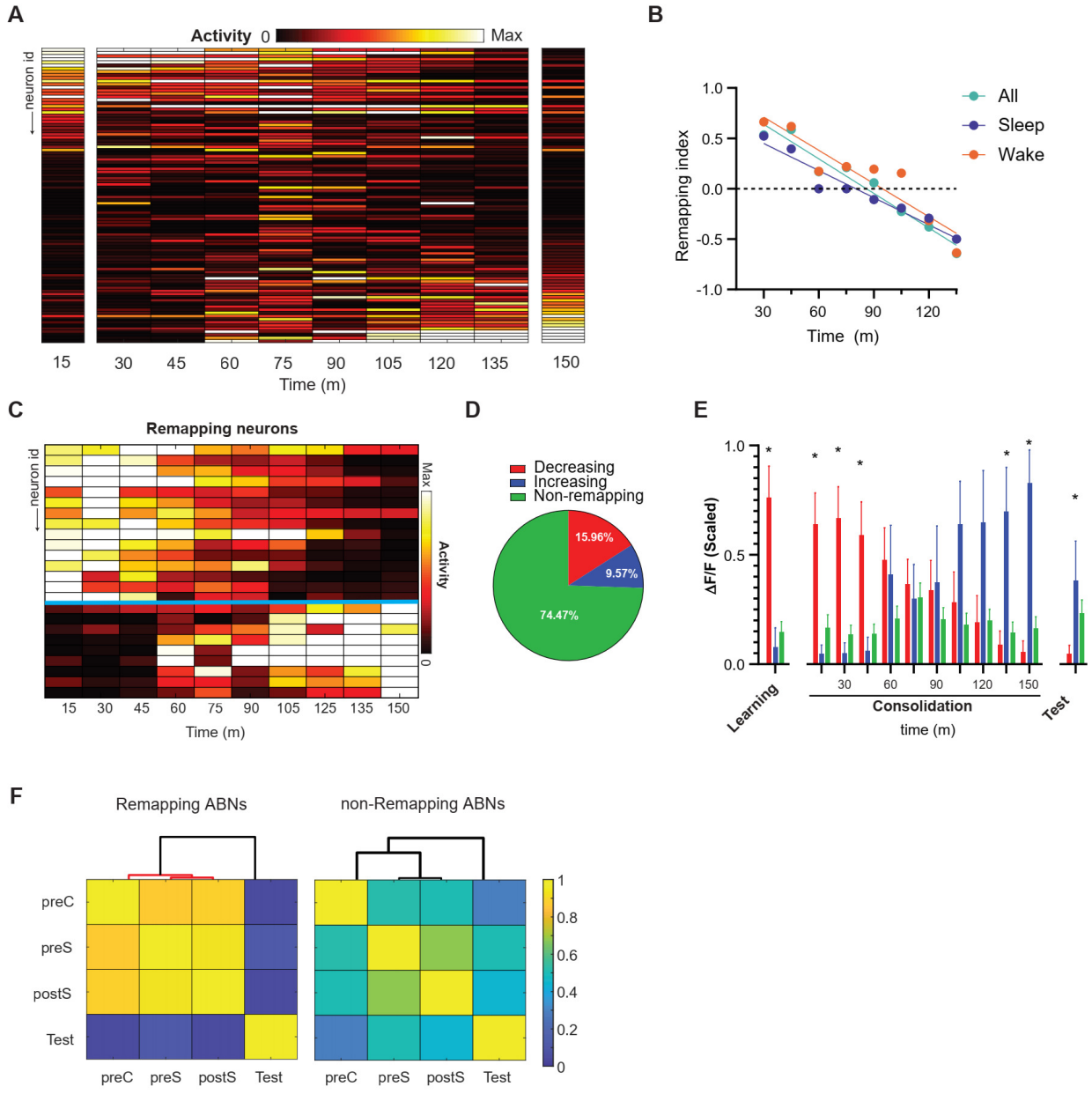

Figure 15. ABN activity remapping during fear memory consolidation. (A) Activity vectors during memory consolidation (15-min bins). To represent data in the same range, the maximum activity of each neuron was scaled to 1. (B) Remapping index relative to the first and last activity vectors shown in (A). All, r= -0.97 p <0.0001; Sleep, r=-0.98 p <0.000; Wake, r=-0.93 p =0.008 (C) Changes in ABN activity were correlated with time (Pearson's correlation, $p < 0.05$; adjusted by false discovery rate, $q < 0.05$). (D) Pie chart of ABNs showing decreasing, increasing, or no change (i.e., non-remapping) in activity over time. (E) Mean activity of remapping and non-remapping ABNs during learning (preS and postS, averaged), consolidation, and test periods. Means were calculated after scaling activity vectors. *$p < 0.05$ between red and blue bars (bootstrap). (F) Similarity matrix between remapping and non-remapping ABNs. Significant clusters (red lines; hierarchical clustering, $p < 0.05$) were found only among remapping ABNs.

8. Discussion

Here we have shown that ABN activities increased when mice explore a novel context, in line with the notion that ABNs act as novelty detectors (Denny et al., 2012; Danielson et al., 2016). However, activity levels dropped back to home cage level after mice received a shock in this context (i.e., post-shock period) (Fanselow, 1980, 1986). On the one hand, this could reflect a lower exploratory activity after the shock experience (i.e. freezing behavior), given that ABNs are predominantly active during running (Danielson et al., 2016). On the other hand, this decrease in activity may reflect changes in the properties of ABNs. For instance, it is well known that contextual fear learning leads to several synaptic changes in ABNs (Kumar, Vergara, et al., 2020; Petsophonsakul et al., 2017). Possibly, contextual fear learning may change the connectivity of ABNs with the inhibitory circuit (Groisman et al., 2020). Indeed, I have recently proposed that an increased coupling with the inhibitory circuits in response to learning may influence how ABN synapses are processed during memory consolidation, presumably by allowing ABNs to coordinate with hippocampal rhythms and enabling spike-timing-dependent synaptic plasticity phenomena in the ABN-entorhinal synapses (Vergara & Sakaguchi, 2020).

Although ABN activity increased when mice explored a new environment, this increase did not represent the recruitment of a specific neural population. Essentially, the same population of ABNs active in the HC was then active in both, the pre- and post-shock periods. In sharp contrast, the ABN activities during memory retrieval did not overlap with the ones during learning. This indicates that ABNs, at least at the population level, do not hold engram properties in a conventional manner (Josselyn and Tonegawa, 2020). Instead, I speculate that ABNs may influence memory by controlling the activity of engram stored in CA3 or the DG (Luna et al., 2019; Temprana et al., 2015). For

instance, ABNs may preferentially recruit inhibitory circuits in CA3 and promote memory discrimination (Rangel et al., 2013; Vergara & Sakaguchi, 2020).

I have found evidence suggesting that the orthogonalization of population activities between learning and retrieval occur as a consequence of a gradual remapping of ABNs activities during the consolidation period. Neurons decreasing their activity during the consolidation period are those that were predominantly active during learning. In contrast, the neurons increasing their activities during the consolidation period were preferentially active during memory retrieval. Although the physiological implication of this remapping process is unknown, I speculate that this remapping process may serve to segregate memories in time (Figure 16). Segregating memories in the timescales of days and weeks is a function that has been previously proposed for ABNs (J. B. Aimone et al., 2006; J. B. B. Aimone et al., 2009; Deng et al., 2010). This activity remapping process may potentially allow ABNs to segregate memories in even shorter time scales (i.e. 6 hours).

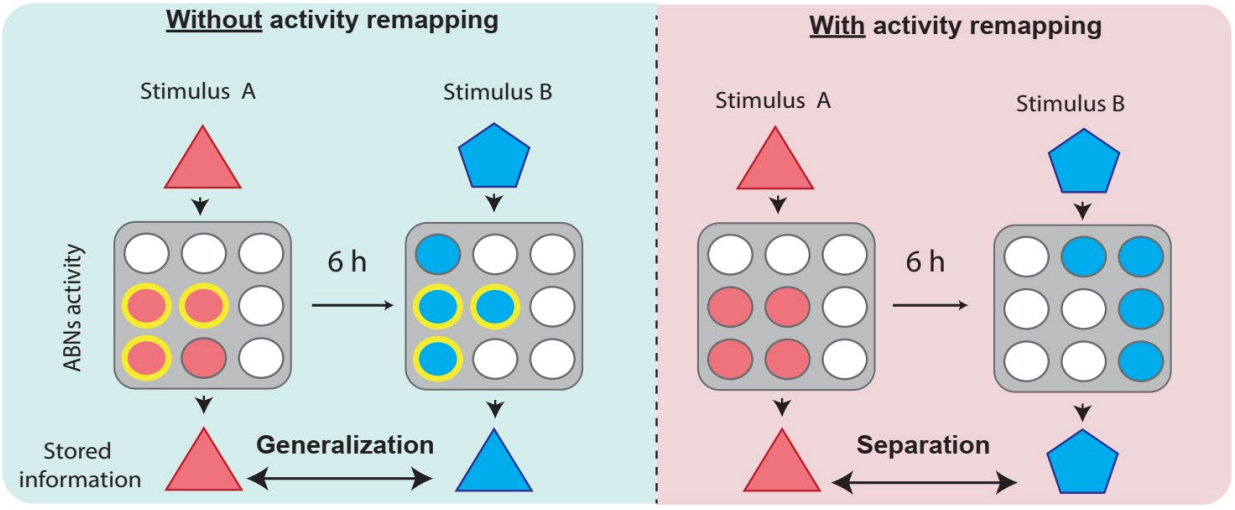

Figure 16. Potential implications of activity remapping. Because ABNs can inhibit or excite other neurons in CA3 and the DG, the population of active ABNs may influence the memory traces that are recruited during the encoding of different memories. In the hypothetical case that activity remapping does not occur (left panel), two different stimuli encoded 6 hours apart would likely compromise overlapping ABNs population during memory encoding, which would promote the generalization of

encoded memories in downstream circuits. In contrast, if there is activity remapping (right panel), different ABNs populations would be engaged during memory encoding, potentially allowing for the separation of memory traces encoded in CA3 or the DG.

One open question is whether the vigilance state of the animal influences activity remapping. A possible approach to address this would be to correlate ABNs activities during individual sleep or wakefulness episodes with activity remapping (Grosmark et al., 2012). However, this approach is unfeasible given the sparse nature of ABNs firing (Kumar, Vergara, et al., 2020). Other important questions include whether ABN activity remapping is learning-dependent and specific to immature ABNs. This can be addressed by an immediate shock experiment, an experimental paradigm in which shock is delivered but there is no context-shock association (Blanchard et al., 1976).

In summary, our results indicate that ABN activity gradually remaps during fear memory consolidation, which leads to the emergence of different ABN populations that are active during learning versus retrieval. This activity remapping may potentially allow ABNs to segregate fear memories encoded a few hours apart. These results advance our understanding of the role of adult neurogenesis in the mammalian memory system.

9. Materials and Methods.

9.1. Experimental model.

The data in this manuscript were obtained by reanalyzing the Ca^{2+} imaging data related to Figure 1I-J in Kumar, Vergara, et al. (2020). The methods used to obtain these data are described in detail by Carrier-Ruiz, Vergara, et al. (2021).

All animal experiments were approved by the University of Tsukuba Institutional Animal Care and Use Committee. Mice were maintained in home cages in an insulated chamber with an ambient temperature of 23.5 ± 2.0°C under a 12-h light/dark cycle

with *ad libitum* access to food and water. Mice (Jackson Laboratory) harboring pNestin-CreER^{T2} (nestin mice, stock #016261) and Rosa26-pCAG-loxP-stop-loxP(LSL)-GCaMP3 (GC mice, Ai38, stock #014538) were backcrossed in a C57BL6/J background more than 10 times. Nestin$^{+/WT}$ mice were bred with GC$^{+/+}$ mice, resulting in F1 GCnestin and GCWT offspring at a nearly 1:1 ratio. Only male F1 mice were used. Mice were habituated to experimenter handling by two or three 2-min handling sessions/day for a total of 11 sessions before behavioral experiments.

To induce GCaMP3 expression in ABNs, all F1 mice were treated with tamoxifen at 7 weeks of age. Tamoxifen (120 mg/kg) was injected into the peritoneal cavity five times at 1- or 2-day intervals, with completion of the injection period within 10 days.

9.2. Implantation of lens and EEG/EMG electrodes.

Surgery was performed at 9 weeks of age. Mice were anesthetized with isoflurane and fixed in a stereotaxic frame (Stoelting, USA). The height of bregma and lambda were adjusted to be equal. The microendoscope lens (1-mm diameter, 4-mm length, Inscopix, USA) was placed at anterior-posterior (AP) -2.0 mm, medial-lateral (ML) +1.2 mm, and dorsal-ventral (DV) -1.95 mm. EEG electrodes were placed at AP +1.5 mm and -3 mm and ML -1.7 mm. EMG electrodes were bilaterally placed into the trapezius muscles. One week after surgery, the baseplate for a miniaturized microendoscope camera (nVista, Inscopix, USA) was attached above the implanted microendoscope lens. Mice were habituated to the attached microendoscope camera for 7-8 days before recording. After each experiment, mice were subject to histological analysis to confirm the location of the lens in the brain.

9.3. Ca^{2+} imaging.

Ca^{2+} imaging was performed at 11 weeks of age. Recordings were done at ZT = ~0. Images were recorded at a rate of 5 frames per second. EEG/EMG data were collected at a sampling rate of 100 Hz. Coaxial electric and optic (Doric Lenses, Canada) slip rings allowed mice to move and sleep naturally.

9.4. Sleep stage analysis.

Offline sleep architecture analysis and Fast Fourier Transform analysis were performed using Sleep Sign software (KISSEI COMTEC). Wakefulness was defined by continuous mouse movement or de-synchronized low-amplitude EEG with tonic EMG activity. NREM sleep was defined by dominant high-amplitude, low-frequency delta waves (1-4 Hz) accompanied by less EMG activity than that observed during wakefulness. REM sleep was defined as dominant theta rhythm (6-9 Hz), and the absence of tonic muscle activity. Vigilant states were defined with a 1 s resolution. If a 1 s epoch contained more than one sleep state (NREM sleep, REM sleep, or wakefulness), the most represented state was assigned for the epoch.

9.5. Fear conditioning and Ca^{2+} imaging.

The fear conditioning chamber consisted of a metal conditioning chamber contained a stainless-steel grid floor (310 x 240 x 210 mm; MED Associates, USA). The grid floor consisted of bars (3.2-mm diameter) spaced 7.9 mm apart allowing the delivery of electric shocks. A stainless-steel drop pan under the grid floor was cleaned with 75% ethanol, which also provided a background odor. The conditioning chamber was placed inside an isolated behavioral chamber to keep the visual and sensory cues constant. A camera was placed at the top of the behavioral chamber and was remotely controlled so that mice could not see the experimenter during context exposure.

Before the fear conditioning experiment, a test recording was done in the home cage to identify mice with significantly active ABNs. At least one active ABNs was detected in 7 out of 17 mice. Mice with active ABNs in the field of view were assigned to a delay shock group, whereas mice displaying no active ABNs were assigned to a no-shock control group. For the delay shock group: on the conditioning day, we attached the microendoscope to mice at ZT = ~0 and performed Ca^{2+} recording for 10 min in the home cage (preC) and an additional 10 min in the fear conditioning chamber (preS) before the foot shock. We then detached the microendoscope (<1 min) to avoid a change in the field of view due to the mouse hitting the microendoscope against the wall during shock. Then, three tones (30 s each, 2800 Hz, 85 dB) were played at 120, 210, and 300 s, with each tone co-terminating with a 2 s foot shock (0.75 mA, 2 s) during a 360 s session. Following, we re-attached the microendoscope (<1 min) and performed 5 min of recording after the shock (postS). Immediately after this recording session, the microscope was removed and mice were returned to the home cage. Subsequently, we performed 2.5 h of recording toward the latter part of the 5.5-h consolidation period in the home cage (consolidation period). Finally, mice were re-exposed to the conditioning context, and Ca^{2+} activity was recorded for 10 min during the memory retrieval (Test). The behavior of the animals was recorded during memory retrieval. Freezing behavior was measured using an automated scoring system (Ohara system) and was defined as a > 1 s continuous absence of movements except for breathing.

Three hours after the memory test, mice were exposed to a novel context consisting of a circular glass chamber (22-cm diameter) with a floor covered with paper and no ethanol odor. Mice did not display freezing behavior in this context (Kumar et al., 2020).

In the case of the no-shock group, mice underwent the same behavioral protocol described for the delay shock group, excepting that a dummy microscope was used, and no shock was delivered during the conditioning period.

9.6. Analysis of Ca^{2+} imaging videos

To extract significant Ca^{2+} transients, recording sessions were concatenated and subsequently motion-corrected in mosaic v1.2 (Inscopix). Fluorescence traces from single neurons were extracted in MATLAB using constrained non-negative matrix factorization for microendoscopic data (CNMF-E) (Zhou et al., 2018). Specific details of the extraction of Ca^{2+} transients are described by Carrier-Ruiz et al. (2021). Ca^{2+} traces were deconvolved using CNMF-E (AR2, thresholded). In this study, only mice with at least 10 ABNs in the field of view were considered (a total of 94 neurons from 4 mice).

Data was analyzed with MATLAB (Mathworks) using the image processing and machine learning toolboxes.

9.6.1. Bootstrap analysis.

Statistical comparison of the means in Figure 13A and Figure 15E was performed by bootstrap analysis. Points were randomly sampled from the original sample to produce a surrogate sample, which was then used to obtain a bootstrap estimate of mean differences between groups. This was repeated 10,000 times to obtain a distribution of different bootstrap estimates. By defining a 1 - α confidence interval within this distribution, I tested whether differences between sample means were statistically different from 0. An α value of 0.05 was divided by the number of multiple comparisons in each experiment (i.e., Bonferroni-corrected). It has been proposed that the bootstrap test may underestimate the expected false positive probability (i.e., Type 1

error) (Bradley Efron & Tibshirani, 1994), especially when sample sizes are small. This issue is addressed in Appendix 1, where I show that the bootstrap approach applied on ABNs data, maintains the type I error in accordance with the hypothetical value of 0.05.

9.6.2. Identification of ABNs responding to novel context exposure.

The mean activity of each neuron in the home cage was compared with its mean activities in preS and postS periods (Figure 13B). The statistical significance of these differences was estimated by moving block bootstrap (Kunsch, 1989). This method differs from classic bootstrap in that blocks of data, rather than individual points, are sampled. This was done to preserve temporal correlations in activity traces (see Appendix 3). The length of the block (10 s) was estimated from the circular autocorrelation function shown in Figure 12B, which reflects the time during which ABN activities were aggregated.

9.6.3. Similarity between activity vectors

The activity vectors in Figure 14B and Figure 15A are the mean activity of individual ABNs arranged in column vectors. To reduce the effect of possible outliers, extreme values for each mouse were truncated to the 95th percentile of the distribution of activities. Data from each mouse were concatenated into a single activity vector. Activity vectors are shown scaled from 0 to 1. The similarity between pairs of activity vectors was estimated by cosine similarity (i.e., normalized dot product), defined as:

$$\cos(A, B) = \frac{A \cdot B}{\|A\|\|B\|} \quad (1)$$

where A and B are two different activity vectors.

9.6.4. Hierarchical clustering.

To identify clusters of activity vectors, I used agglomerative hierarchical clustering. Clusters were combined using angular distance (i.e., cosine distance) and Wards linkage. Statistically significant cut-off points in the dendrogram were estimated on the basis of a reference distribution of linkages obtained by random resampling of activity vectors (10,000 replicates) (Sebastiani & Perls, 2016).

9.6.5. Remapping index.

The remapping index (RI) is defined as:

$$\mathrm{RI} = \frac{AD(A, B^t) - AD(C, B^t)}{AD(A, B^t) + AD(C, B^t)} \quad (2)$$

Where AD is the angular distance, which is equal to 1 - cosine similarity value, A and C are the activity vectors from the first and last 15 min of the consolidation period, respectively, and B^t is the activity vector at time t.

10. Funding.

This work was partially supported by grants from the World Premier International Research Center Initiative from MEXT, JST CREST grant #JPMJCR1655, JSPS KAKENHI grants #16K18359, 15F15408, 26115502, 25116530, JP16H06280, 19F19310, and 20H03552, Shimadzu Science Foundation, The Uehara Memorial Foundation, Takeda Science Foundation, Kanae Foundation, Research Foundation for Opto-Science and Technology, Ichiro Kanehara Foundation, Kato Memorial Bioscience Foundation, Japan Foundation for Applied Enzymology, Senshin Medical Research Foundation, Life Science Foundation of Japan, Brain Science Foundation, Kowa Life Science Foundation, Inamori Research Grants Program, and GSK Japan to M.S.

11. Institutional Review Board Statement.

All experiments were performed in accordance with the Science Council of Japan's Guidelines for Proper Conduct of Animal Experiments. All experimental protocols that involved animals were approved by the University of Tsukuba Institutional Animal Care and Use Committee [Protocol#20-268] and the Recombinant DNA Use Committee [Protocol#180089 and 190035].

12. Data Availability Statement.

The data (raw Ca^{2+} transients and activity traces) and the code supporting the finding of this study (MATLAB) are available at:

https://github.com/vergaloy/Remapping_ABNs

13. Acknowledgments.

I am very grateful to Dr. Sakaguchi for his patience and enthusiasm. I would also like to thank my previous mentor Dr. Magdalena Sanhueza who formed me as a scientist. Finally, I would like to thank my parents, who raised me and made me the person I am today.

14. Appendix.

14.1. Appendix 1. Controlling bootstrap Type I error.

Bootstrap analysis was used to compare the activity vectors shown in Figure 13A and Figure 15E. These activity vectors are lognormally distributed and zero-inflated (e.g., ~30% of the ABNs are completely inactive in the home cage condition) (Figure 17A). Commonly used statistical approaches, such as t-test or Wilcoxon-Mann-Whitney test, may not perform well in these conditions (McElduff et al., 2010). To address this issue, I used bootstrap (Efron, 1979, see section 8.6.1). One of the main advantages of using bootstrap for statistical inference is that it is asymptotically more accurate than a t-test

when assumptions of normality and equality of variance between conditions are not met (DiCiccio & Efron, 1996). The main disadvantage is that its accuracy is limited to the representative sample (i.e., is biased). If the representative sample is small, the number of possible bootstrap replicates that can be produced may not be rich enough to represent the parameter of interest (B. Efron, 1979). For example, when means are compared in normally distributed data, the bootstrap approach display higher false-positive probability (type I error) when the number of samples is very small (Efron, 1979, N <50). One usual way to calculate the type I error of resampling approaches, such as bootstrap, is to run the resampling test several times on simulated data (Boos & Zhang, 2000). For example, the type I error of the bootstrap test for normally distributed data (Figure 17B) can be calculated as follows:

1) N data points are randomly sampled from a normal distribution (mean = 0, standard deviation = 1), and assigned to two different groups.

2) The sample means between these two groups are then compared by bootstrap. The result of the statistical test is stored (reject the null hypothesis?).

3) This process is repeated 1000 times.

Because samples were obtained from the same normal distribution, counting the number of times that the null hypothesis was rejected can serve to estimate the false-positive probability (type I error) of the bootstrap test. This simulation shows that, for normally distributed data, the observed type I error converges to the hypothetical value ($\alpha = 0.05$) when the sample size is above 40.

The example illustrated above shows the type I error for normally distributed data. To calculate the bootstrap type I error in our data (96 ABNs, non-normally distributed), instead of sampling from a normal distribution, data points were pseudo-randomly produced by sampling from the empirical cumulative probability density function of

ABNs activities (shown in Figure 17A, right). Therefore, the produced bootstrap replicates were lognormally distributed and zero-inflated as occurring with the actual mean-ΔF/F data. The estimated type I error corresponded to the theoretical value of α = 0.05 (Figure 17C), corroborating that bootstrap does not underestimate the number of false positives.

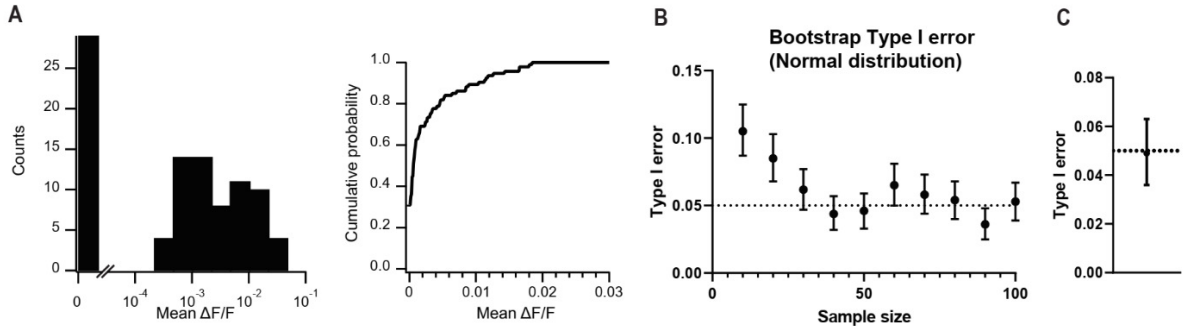

Figure 17. Estimating type I error in bootstrap. (A) Left: Histogram of the mean ΔF/F of 96 ABNs in home cage. Right: Empiric cumulative probability density function of the mean ΔF/F (B) Example showing type I error produced by the bootstrap test for different sample sizes (only for normally distributed data). (C) Type I error for ABNs data.

14.2. Appendix 2. Bootstrap for temporally correlated data.

Bootstrap analysis was also used to detect changes in the mean activity of individual ABNs (i.e., data in Figure 13B). In this case, the question to address is whether the mean activity of a neuron is different in two conditions. For example, Figure 18A shows the activity traces of the same neuron in two different contexts. The conventional bootstrap approach will not be appropriate in this case, because Ca^{2+} traces in ABNs display burst-like activity. Therefore, random sampling without considering the temporal structure of the data would not preserve the bursting activity in the bootstrap replicates (Figure 18B). Instead of using the conventional bootstrap approach, I used the box bootstrap approach proposed by Kunsch, 1989, in which consecutive points

of data (i.e., boxes of data) are randomly sampled instead of individual points. This allows preserving the bursting profile of ABNs Ca^{2+} traces (Figure 18B, left). Indeed, the box bootstrap surrogates and the original samples display a similar average autocorrelation function (Figure 18B, right), indicating that the box bootstrap preserves the burstiness of the original data.

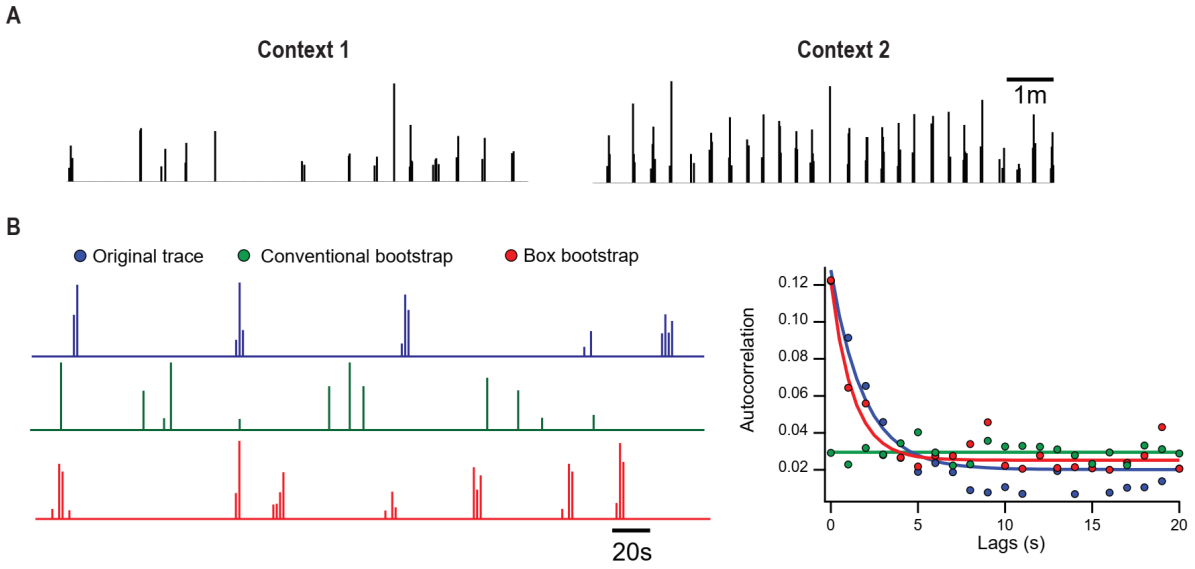

Figure 18. The box bootstrap approach preserves the burstiness of the original traces. (A) Ca^{2+} activity traces of the same neuron in two different contexts. (B) Conventional bootstrap vs box bootstrap. Left: original trace (blue); conventional bootstrap replicate (green); box bootstrap replicate (red). Note that the box bootstrap replicate preserves the burstiness of the original trace. Right: mean autocorrelation function for the original data (blue), for surrogate data produced by conventional bootstrap (green), and for surrogate data produced by box bootstrap (Red).

14.3. Appendix 3. Remapping can be detected in individual mice.

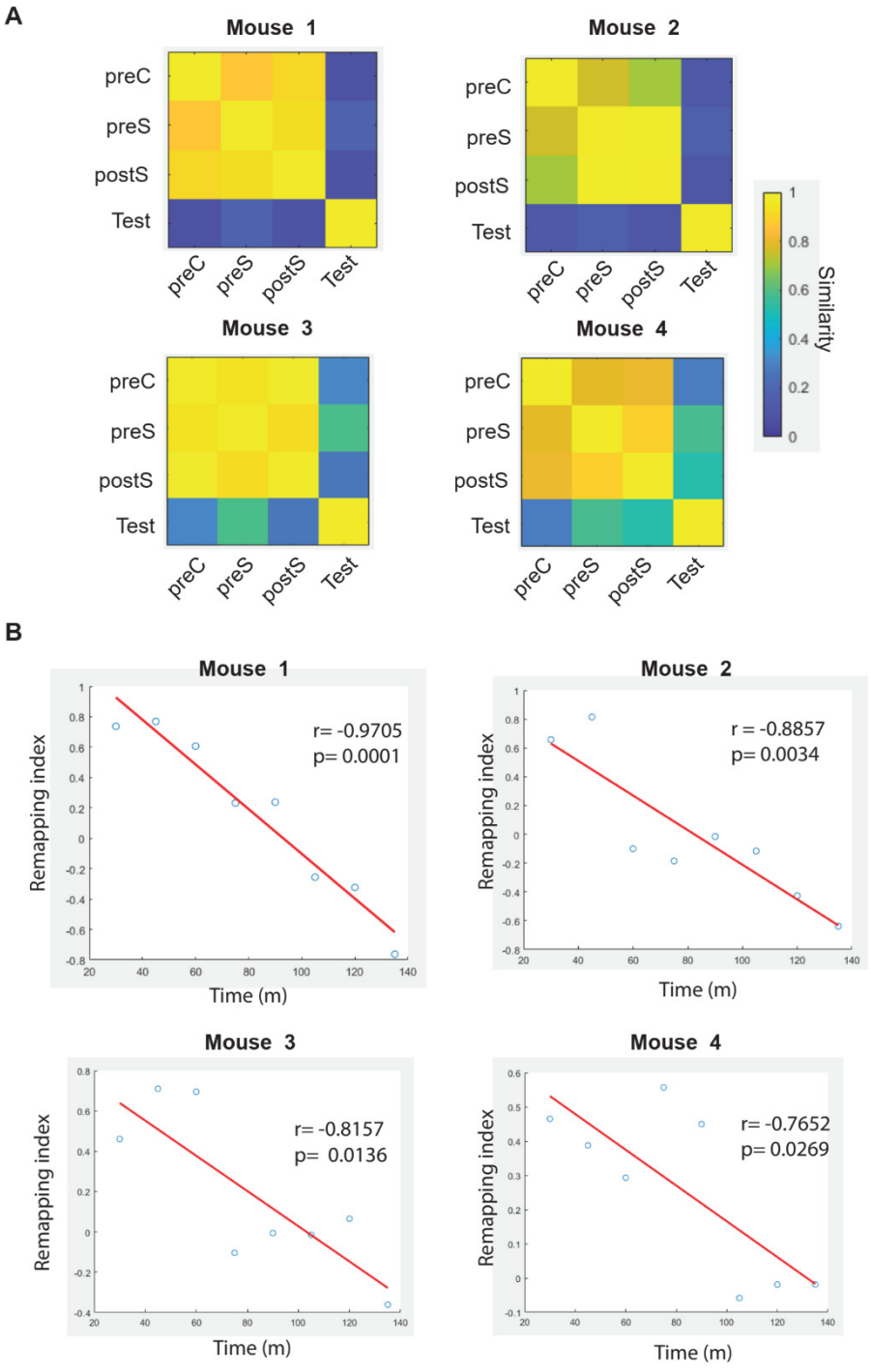

Figure 19. Remapping can be detected in individual mice. (A) Similarity matrix of the activity vectors of each mouse. (B) Remapping index vs time correlation for each mouse. The number of neurons in each mouse is n= 37, 30, 13, and 14.

15. References

Aharoni, D., & Hoogland, T. M. (2019). Circuit Investigations With Open-Source Miniaturized Microscopes: Past, Present and Future. *Frontiers in Cellular Neuroscience*, *13*. https://doi.org/10.3389/fncel.2019.00141

Aharoni, D., Khakh, B. S., Silva, A. J., & Golshani, P. (2019). All the light that we can see: a new era in miniaturized microscopy. *Nature Methods*, *16*(1), 11–13. https://doi.org/10.1038/s41592-018-0266-x

Aimone, J. B. B., Wiles, J., & Gage, F. H. H. (2009). Computational Influence of Adult Neurogenesis on Memory Encoding. *Neuron*, *61*(2), 187–202. https://doi.org/10.1016/j.neuron.2008.11.026

Aimone, J. B., Wiles, J., & Gage, F. H. (2006). Potential role for adult neurogenesis in the encoding of time in new memories. *Nature Neuroscience*, *9*(6), 723–727. https://doi.org/10.1038/nn1707

Aljadeff, J., Lansdell, B. J., Fairhall, A. L., & Kleinfeld, D. (2016). Analysis of Neuronal Spike Trains, Deconstructed. In *Neuron* (Vol. 91, Issue 2, pp. 221–259). Cell Press. https://doi.org/10.1016/j.neuron.2016.05.039

Altman, J. (1963). Autoradiographic investigation of cell proliferation in the brains of rats and cats. *The Anatomical Record*, *145*(4), 573–591. https://doi.org/10.1002/ar.1091450409

Alvarez, D. D. D., Giacomini, D., Yang, S. M. M., Trinchero, M. F. F., Temprana, S. G. G., Buttner, K. A., Beltramone, N., Schinder, A. F. F., Büttner, K. A., Beltramone, N., & Schinder, A. F. F. (2016). A disynaptic feedback network activated by experience promotes the integration of new granule cells. *Science*, *354*(6311), 459–465. https://doi.org/10.1126/science.aaf2156

Arruda-Carvalho, M., Sakaguchi, M., Akers, K. G., Josselyn, S. A., & Frankland, P. W. (2011). Posttraining Ablation of Adult-Generated Neurons Degrades Previously Acquired Memories. *Journal of Neuroscience*, *31*(42), 15113–15127. https://doi.org/10.1523/JNEUROSCI.3432-11.2011

Berridge, M. J., Lipp, P., & Bootman, M. D. (2000). The versatility and universality of calcium signalling. *Nature Reviews Molecular Cell Biology*, *1*(1), 11–21. https://doi.org/10.1038/35036035

Boos, D. D., & Zhang, J. (2000). Monte Carlo Evaluation of Resampling-Based Hypothesis Tests. *Journal of the American Statistical Association*, *95*(450), 486–492. https://doi.org/10.1080/01621459.2000.10474226

Danielson, N. B. B., Kaifosh, P., Zaremba, J. D. D., Lovett-Barron, M., Tsai, J., Denny, C. A. A., Balough, E. M. M., Goldberg, A. R. R., Drew, L. J. J., Hen, R., Losonczy, A., & Kheirbek, M. A. A. (2016). Distinct Contribution of Adult-Born Hippocampal Granule Cells to Context Encoding. *Neuron*, *90*(1), 101–112. https://doi.org/10.1016/j.neuron.2016.02.019

Deng, W., Aimone, J. B., & Gage, F. H. (2010). New neurons and new memories: how does adult hippocampal neurogenesis affect learning and memory? *Nature Reviews. Neuroscience*, *11*(5), 339–350. https://doi.org/10.1038/nrn2822

Diamantaki, M., Frey, M., Berens, P., Preston-Ferrer, P., & Burgalossi, A. (2016). Sparse activity of identified dentate granule cells during spatial exploration. *ELife*, *5*(OCTOBER2016). https://doi.org/10.7554/eLife.20252.001

DiCiccio, T. J., & Efron, B. (1996). Bootstrap confidence intervals. *Statistical Science*, *11*(3), 181–188. https://doi.org/10.1214/ss/1032280214

Efron, B. (1979). Bootstrap Methods: Another Look at the Jackknife. *The Annals of Statistics*, *7*(1), 1403–1433. https://doi.org/10.1214/aos/1176344552

Efron, Bradley, & Tibshirani, R. J. (1994). An Introduction to the Bootstrap. In *An Introduction to the Bootstrap*. Chapman and Hall/CRC. https://doi.org/10.1201/9780429246593

Esposito, M. S. (2005). Neuronal Differentiation in the Adult Hippocampus Recapitulates Embryonic Development. *Journal of Neuroscience*, *25*(44), 10074–10086. https://doi.org/10.1523/JNEUROSCI.3114-05.2005

Friedrich, J., Zhou, P., & Paninski, L. (2017). Fast online deconvolution of calcium imaging data. *PLoS Computational Biology*, *13*(3), 1–26. https://doi.org/10.1371/journal.pcbi.1005423

Ge, S., Yang, C. hao, Hsu, K. sen, Ming, G. li, & Song, H. (2007). A Critical Period for Enhanced Synaptic Plasticity in Newly Generated Neurons of the Adult Brain. *Neuron*, *54*(4), 559–566. https://doi.org/10.1016/j.neuron.2007.05.002

Ghosh, K. K., Burns, L. D., Cocker, E. D., Nimmerjahn, A., Ziv, Y., Gamal, A. El, & Schnitzer, M. J. (2011). Miniaturized integration of a fluorescence microscope. *Nature Methods*, *8*(10), 871–878. https://doi.org/10.1038/nmeth.1694

Groisman, A. I., Yang, S. M., & Schinder, A. F. (2020). Differential Coupling of Adult-Born Granule Cells to Parvalbumin and Somatostatin Interneurons. *Cell Reports*, *30*(1), 202-214.e4. https://doi.org/10.1016/j.celrep.2019.12.005

Grosmark, A. D., Mizuseki, K., Pastalkova, E., Diba, K., & Buzsáki, G. (2012). REM Sleep Reorganizes Hippocampal Excitability. *Neuron*, *75*(6), 1001–1007. https://doi.org/10.1016/j.neuron.2012.08.015

Gu, Y., Arruda-Carvalho, M., Wang, J., Janoschka, S. R., Josselyn, S. A., Frankland, P. W., & Ge, S. (2012). Optical controlling reveals time-dependent roles for adult-born dentate granule cells. *Nature Neuroscience*, *15*(12), 1700–1706. https://doi.org/10.1038/nn.3260

Henze, D. A., Wittner, L., & Buzsáki, G. (2002). Single granule cells reliably discharge targets in the hippocampal CA3 network in vivo. *Nature Neuroscience*, *5*(8), 790–795. https://doi.org/10.1038/nn887

Josselyn, S. A., & Tonegawa, S. (2020). Memory engrams: Recalling the past and imagining the future. *Science*, *367*(6473), eaaw4325. https://doi.org/10.1126/science.aaw4325

Kumar, D., Koyanagi, I., Carrier-Ruiz, A., Vergara, P., Srinivasan, S., Sugaya, Y., Kasuya, M., Yu, T.-S., Vogt, K. E. E., Muratani, M., Ohnishi, T., Singh, S., Teixeira, C. M. M., Chérasse, Y., Naoi, T., Wang, S., Nondhalee, P., Osman, B. A. A. H., Kaneko, N., … Sakaguchi, M. (2020). Sparse Activity of Hippocampal Adult-Born Neurons during REM Sleep Is Necessary for Memory Consolidation.

Neuron, *107*(3), 552-565.e10. https://doi.org/10.1016/j.neuron.2020.05.008

Kunsch, H. R. (1989). The Jackknife and the Bootstrap for General Stationary Observations. *The Annals of Statistics*, *17*(3), 1217–1241. https://doi.org/10.1214/aos/1176347265

Luna, V. M., Anacker, C., Burghardt, N. S., Khandaker, H., Andreu, V., Millette, A., Leary, P., Ravenelle, R., Jimenez, J. C., Mastrodonato, A., Denny, C. A., Fenton, A. A., Scharfman, H. E., & Hen, R. (2019). Adult-born hippocampal neurons bidirectionally modulate entorhinal inputs into the dentate gyrus. *Science*, *364*(6440), 578–583. https://doi.org/10.1126/science.aat8789

Madisen, L., Garner, A. R., Shimaoka, D., Chuong, A. S., Klapoetke, N. C., Li, L., van der Bourg, A., Niino, Y., Egolf, L., Monetti, C., Gu, H., Mills, M., Cheng, A., Tasic, B., Nguyen, T. N., Sunkin, S. M., Benucci, A., Nagy, A., Miyawaki, A., … Zeng, H. (2015). Transgenic Mice for Intersectional Targeting of Neural Sensors and Effectors with High Specificity and Performance. *Neuron*, *85*(5), 942–958. https://doi.org/10.1016/j.neuron.2015.02.022

McElduff, F., Cortina-Borja, M., Chan, S.-K., & Wade, A. (2010). When t -tests or Wilcoxon-Mann-Whitney tests won't do. *Advances in Physiology Education*, *34*(3), 128–133. https://doi.org/10.1152/advan.00017.2010

Moreira, P. S., Almeida, P. R., Leite-Almeida, H., Sousa, N., & Costa, P. (2016). Impact of Chronic Stress Protocols in Learning and Memory in Rodents: Systematic Review and Meta-Analysis. *PLOS ONE*, *11*(9), e0163245. https://doi.org/10.1371/journal.pone.0163245

Nollet, M., Hicks, H., McCarthy, A. P., Wu, H., Möller-Levet, C. S., Laing, E. E., Malki, K., Lawless, N., Wafford, K. A., Dijk, D.-J., & Winsky-Sommerer, R. (2019). REM sleep's unique associations with corticosterone regulation, apoptotic pathways, and behavior in chronic stress in mice. *Proceedings of the National Academy of Sciences*, *116*(7), 2733–2742. https://doi.org/10.1073/pnas.1816456116

Orr, G., Rao, G., Houston, F. P., McNaughton, B. L., & Barnes, C. A. (2001). Hippocampal synaptic plasticity is modulated by theta rhythm in the fascia dentata of adult and aged freely behaving rats. *Hippocampus*, *11*(6), 647–654. https://doi.org/10.1002/hipo.1079

Petsophonsakul, P., Richetin, K., Andraini, T., Roybon, L., & Rampon, C. (2017). Memory formation orchestrates the wiring of adult-born hippocampal neurons into brain circuits. *Brain Structure and Function*, *222*(6), 2585–2601. https://doi.org/10.1007/s00429-016-1359-x

Pnevmatikakis, E. A., & Giovannucci, A. (2017). NoRMCorre: An online algorithm for piecewise rigid motion correction of calcium imaging data. *Journal of Neuroscience Methods*, *291*, 83–94. https://doi.org/10.1016/j.jneumeth.2017.07.031

Praag, H. Van, Gage, F. H. H., Schinder, A. F. F., Laplagne, D. A., Espósito, M. S., Piatti, V. C., Morgenstern, N. A., Zhao, C., van Praag, H., Gage, F. H. H., & Schinder, A. F. F. (2006). Functional Convergence of Neurons Generated in the Developing and Adult Hippocampus. *PLoS Biology*, *4*(12), e409.

https://doi.org/10.1371/journal.pbio.0040409

Rangel, L. M., Quinn, L. K., Chiba, A. A., Gage, F. H., & Aimone, J. B. (2013). A hypothesis for temporal coding of young and mature granule cells. *Frontiers in Neuroscience*, *7 MAY*, 2000–2009. https://doi.org/10.3389/fnins.2013.00075

Rey, H. G., Pedreira, C., & Quian Quiroga, R. (2015). Past, present and future of spike sorting techniques. *Brain Research Bulletin*, *119*, 106–117. https://doi.org/10.1016/j.brainresbull.2015.04.007

Schmidt-Hieber, C., Jonas, P., & Bischofberger, J. (2004). Enhanced synaptic plasticity in newly generated granule cells of the adult hippocampus. *Nature*, *429*(6988), 184–187. https://doi.org/10.1038/nature02553

Sebastiani, P., & Perls, T. T. (2016). Detection of significant groups in hierarchical clustering by resampling. *Frontiers in Genetics*, *7*(AUG). https://doi.org/10.3389/fgene.2016.00144

Semon, R. (1921). *The mnem*. London: George Allen & Unwin.

Shors, T. J., Miesegaes, G., Beylin, A., Zhao, M., Rydel, T., & Gould, E. (2001). Erratum: correction: Neurogenesis in the adult is involved in the formation of trace memories. *Nature*, *414*(6866), 938–938. https://doi.org/10.1038/414938a

Srinivasan, S., Hosokawa, T., Vergara, P., Chérasse, Y., Naoi, T., Sakurai, T., & Sakaguchi, M. (2019). Miniaturized microscope with flexible light source input for neuronal imaging and manipulation in freely behaving animals. *Biochemical and Biophysical Research Communications*, *517*(3), 520–524. https://doi.org/10.1016/j.bbrc.2019.07.082

Stone, S. S. D., Teixeira, C. M., Zaslavsky, K., Wheeler, A. L., Martinez-Canabal, A., Wang, A. H., Sakaguchi, M., Lozano, A. M., & Frankland, P. W. (2011). Functional convergence of developmentally and adult-generated granule cells in dentate gyrus circuits supporting hippocampus-dependent memory. *Hippocampus*, *21*(12), 1348–1362. https://doi.org/10.1002/hipo.20845

Temprana, S. G., Mongiat, L. A., Yang, S. M., Trinchero, M. F., Alvarez, D. D., Kropff, E., Giacomini, D., Beltramone, N., Lanuza, G. M., & Schinder, A. F. (2015). Delayed Coupling to Feedback Inhibition during a Critical Period for the Integration of Adult-Born Granule Cells. *Neuron*, *85*(1), 116–130. https://doi.org/10.1016/j.neuron.2014.11.023

Thomas, M. J., Watabe, A. M., Moody, T. D., Makhinson, M., & O'Dell, T. J. (1998). Postsynaptic complex spike bursting enables the induction of LTP by theta frequency synaptic stimulation. *Journal of Neuroscience*, *18*(18), 7118–7126. https://doi.org/10.1523/jneurosci.18-18-07118.1998

Tian, L., Hires, S. A., Mao, T., Huber, D., Chiappe, M. E., Chalasani, S. H., Petreanu, L., Akerboom, J., McKinney, S. A., Schreiter, E. R., Bargmann, C. I., Jayaraman, V., Svoboda, K., & Looger, L. L. (2009). Imaging neural activity in worms, flies and mice with improved GCaMP calcium indicators. *Nature Methods*, *6*(12), 875–881. https://doi.org/10.1038/nmeth.1398

Vergara, P., & Sakaguchi, M. (2020). Mechanisms Underlying Memory Consolidation by Adult-Born Neurons During Sleep. *Frontiers in Cellular Neuroscience*,

14(November), 1–7. https://doi.org/10.3389/fncel.2020.594401

Zhou, P., Resendez, S. L., Rodriguez-Romaguera, J., Jimenez, J. C., Neufeld, S. Q., Giovannucci, A., Friedrich, J., Pnevmatikakis, E. A., Stuber, G. D., Hen, R., Kheirbek, M. A., Sabatini, B. L., Kass, R. E., & Paninski, L. (2018). Efficient and accurate extraction of in vivo calcium signals from microendoscopic video data. *ELife*, *7*, 1–37. https://doi.org/10.7554/eLife.28728

16. Source

The contents previously published in “Vergara, P.; Kumar, D.; Srinivasan, S.; Koyanagi, I.; Naoi, T.; Singh, S.; Sakaguchi, M. Remapping of Adult-Born Neuron Activity during Fear Memory Consolidation in Mice. Int. J. Mol. Sci. 2021, 22, 2874, doi:10.3390/ijms22062874” are re-used in this dissertation following the guidance from Multidisciplinary Digital Publishing Institute (open access article under the CC BY license, http://creativecommons.org/licenses/by/4.0/).

The contents previously published in “Carrier-Ruiz, A.; Sugaya, Y.; Kumar, D.; Vergara, P.; Koyanagi, I.; Srinivasan, S.; Naoi, T.; Kano, M.; Sakaguchi, M. Calcium imaging of adult-born neurons in freely moving mice. STAR Protoc. 2021, 2, 100238, doi:10.1016/j.xpro.2020.100238.” are re-used in this dissertation following the guidance from Cell Press (open access article under the CC BY license, http://creativecommons.org/licenses/by/4.0/).